



Article

Bi-Functional Paraffin@Polyaniline/TiO₂/PCN-222(Fe) Microcapsules for Solar Thermal Energy Storage and CO₂ Photoreduction

Wenchang Sun, Yueming Hou and Xu Zhang *

Hebei key Laboratory of Functional Polymers, School of Chemical Engineering and Technology, Hebei University of Technology, Tianjin 300130, China; 201811501015@stu.hebut.edu.cn (W.S.); 201921501013@stu.hebut.edu.cn (Y.H.)

* Correspondence: xuzhang@hebut.edu.cn; Tel./Fax: +86-22-6020-0443

Abstract: A novel type of bi-functional microencapsulated phase change material (MEPCM) microcapsules with thermal energy storage (TES) and carbon dioxide (CO₂) photoreduction was designed and fabricated. The polyaniline (PANI)/titanium dioxide (TiO₂)/PCN-222(Fe) hybrid shell encloses phase change material (PCM) paraffin by the facile and environment-friendly Pickering emulsion polymerization, in which TiO₂ and PCN-222(Fe) nanoparticles (NPs) were used as Pickering stabilizer. Furthermore, a ternary heterojunction of PANI/(TiO₂)/PCN-222(Fe) was constructed due to the tight contact of the three components on the hybrid shell. The results indicate that the maximum enthalpy of MEPCMs is 174.7 J·g⁻¹ with encapsulation efficiency of 77.2%, and the thermal properties, chemical composition, and morphological structure were well maintained after 500 high–low temperature cycles test. Besides, the MEPCM was employed to reduce CO₂ into carbon monoxide (CO) and methane (CH₄) under natural light irradiation. The CO evolution rate reached up to 45.16 μmol g⁻¹ h⁻¹ because of the suitable band gap and efficient charge migration efficiency, which is 5.4, 11, and 62 times higher than pure PCN-222(Fe), PANI, and TiO₂, respectively. Moreover, the CO evolution rate decayed inapparently after five CO₂ photoreduction cycles. The as-prepared bi-functional MEPCM as the temperature regulating building materials and air purification medium will stimulate a potential application.

Keywords: microencapsulated phase change material; solar thermal energy storage; Pickering emulsion polymerization; CO₂ photoreduction



Citation: Sun, W.; Hou, Y.; Zhang, X. Bi-Functional Paraffin@Polyaniline/TiO₂/PCN-222(Fe) Microcapsules for Solar Thermal Energy Storage and CO₂ Photoreduction. *Nanomaterials* **2022**, *12*, 2. <https://doi.org/10.3390/nano12010002>

Academic Editor: Woo Kyoung Kim and Christian M. Julien

Received: 28 October 2021

Accepted: 17 December 2021

Published: 21 December 2021

Publisher's Note: MDPI stays neutral with regard to jurisdictional claims in published maps and institutional affiliations.



Copyright: © 2021 by the authors. Licensee MDPI, Basel, Switzerland. This article is an open access article distributed under the terms and conditions of the Creative Commons Attribution (CC BY) license (<https://creativecommons.org/licenses/by/4.0/>).

1. Introduction

Energy and environmental issues have become two crucial obstacles restricting the construction of low-carbon energy systems [1]. Thermal energy storage (TES) is a clean and effective technology to solve the environmental crisis and reduce consumption of fossil fuels [2]. Phase change materials (PCMs), such as organics (paraffin, fatty acids, esters, alcohols, and glycols), inorganics (salt hydrates or metallic), and eutectics (mixtures of inorganic and organic), act a pivotal part in the sustainable progress of economic development under the background of increasing energy consumption due to the valuable heat storage capability, physical-chemistry durability, and small volume change [3,4]. PCMs can store heat energy at high temperatures and then release heat energy at low-temperature conditions, which shows excellent application potential in thermal insulation materials, thermo-regulated textiles, photothermal conversion, etc. [5–7]. However, the leakage and poor thermal conductivity of PCMs during the high–low temperature change limits the direct application under practical conditions [8]. Therefore, many encapsulated technologies (microcapsules, porous materials adsorption, blending, etc.) for confining PCMs have been developed to overcome the leakage [9–11].

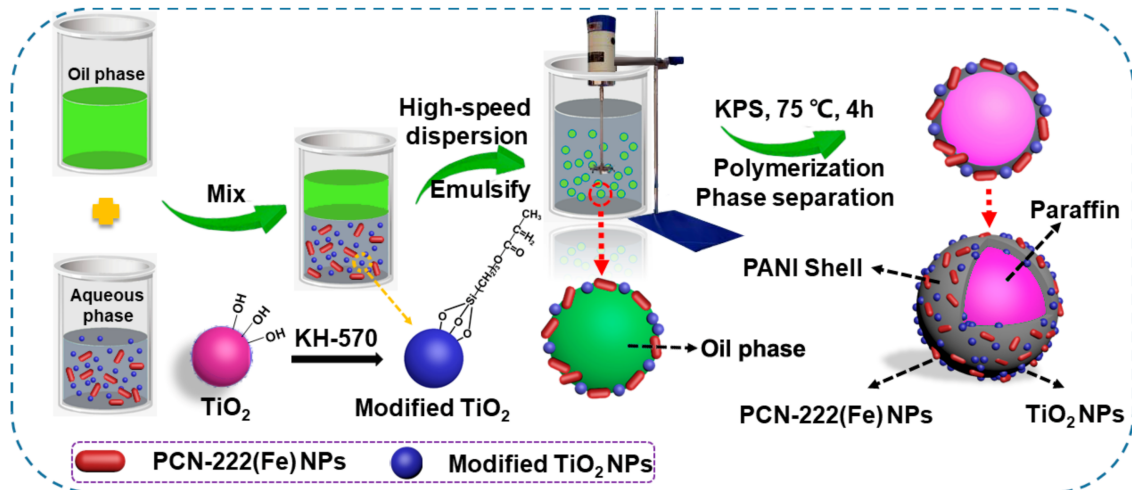
Microencapsulation is one of the main methods of fabricating core-shell structures, where the PCMs as the core materials are confined by the shell material [12]. Generally,

monolayer polymeric or inorganic shell materials were used to fabricate microencapsulated PCMs (MEPCMs). However, there are some defects that exist in the microencapsulated PCMs with polymeric shells, such as flammable properties, inferior thermos-stability, and defective thermal conductivity. In addition, the MEPCMs with inorganic shells also possess shortages of poor mechanical properties and low encapsulation efficiency [13]. Satisfactorily, MEPCMs with organic–inorganic hybrid shells integrate the superiorities and avoid the shortcomings of a single kind of shell to the most extent [14–16]. Nowadays, various technologies have been employed to fabricate MEPCMs with organic–inorganic hybrid shells; Pickering emulsion polymerization has been a trend to prepare MEPCMs because of its facile, nontoxic, and environmentally-friendly features, in which there is no need to add molecular emulsifiers and the pollution to the environment is also avoided [17].

Among the various prepared MEPCMs microcapsules, the multi-functional MEPCMs have aroused an increasing research interest [18,19]. The multi-functionality of MEPCMs can be achieved in the following three ways: (1) embedding nanoparticles (NPs) into the shell, (2) utilizing function-specific shell materials, and (3) designing the shape of the microcapsule [18]. Typically, one way was employed to prepare the multi-functional MEPCMs, for instance, the functional NPs ferric oxide (Fe_2O_3), titanium dioxide (TiO_2), zinc oxide (ZnO), metal–organic frameworks (MOFs), and were embedded into the polymeric shell, or the functional inorganic shells like TiO_2 , cuprous oxide (Cu_2O), tin dioxide (SnO_2), and cadmium sulfide (CdS) were directly used for the shell to achieve the UV shielding, fluorescent, photothermal conversion, photocatalysis, antibacterial, and thermal conduction, etc. [20–28]. In our previous work [29], a kind of MEPCM with TiO_2 /PDVB hybrid shell was fabricated by Pickering emulsion polymerization; nevertheless, the use efficiency of single functional TiO_2 NPs in the MEPCM is relatively low, nonfunctional PDVB shell could not achieve a synergetic combination of NPs and shell for further improving the multi-functionality especially the photocatalysis. Thus, by selecting suitable NPs and shell materials to construct heterojunction on the microcapsule, the various components can be fully contacted and entirely integrated. Every single functional component can achieve the elevated effect or new properties that are not available from a single component.

Herein, a novel bi-functional MEPCMs consisting of a paraffin core and a PCN-222(Fe)/titanium dioxide/polyaniline hybrid shell was prepared for solar photocatalysis and thermal storage. In the past, the polymer shell had no function other than as a shell material. Polyaniline (PANI) as the conductive polymer has attracted extensive attention because of its strong light absorption capacity and excellent photothermal conversion in a range of natural regions. However, the photocatalytic ability of PANI is restricted due to the rapid carrier recombination [30]. TiO_2 is a kind of UV-responsive semiconductor with a high electron/hole pair complexation probability, limiting solar energy utilization for photocatalysis [31]. Moreover, numerous reports have confirmed that MOFs are excellent materials for photocatalysis, such as UiO-based MOFs, MIL-based MOFs, ZIFs-based MOFs, and Porphyrin-based MOFs [32–39] Porphyrin MOFs, such as PCN-222(Fe), are porous coordination materials formed by linking metalloporphyrins with metal carboxylate clusters [40]. However, the energy-level alignment defects and asymmetry make porphyrin MOFs have inferior photocatalytic efficiency [41]. The combination of several materials to form a heterojunction can significantly enhance the natural light absorption intensity, absorption range, and photogenerated charge migration efficiency at the interface for improving photocatalytic efficiency [42]. Therefore, a method of constructing ternary heterojunction on the surface of the organic–inorganic hybrid shell layer of MEPCMs was proposed; the detailed preparation process is shown in Scheme 1. A green Pickering emulsion polymerization was used for microencapsulating PCM with PANI/ TiO_2 /PCN-222(Fe) hybrid shell, where PCN-222(Fe) and KH-570 modified TiO_2 NPs were used as Pickering emulsion stabilizers. PCN-222(Fe) and TiO_2 NPs were dispersed and embedded on the PANI shell after polymerization, in which the three components are contacted tightly mutually to construct a ternary heterojunction shell. The fabricated paraffin@PANI/ TiO_2 /PCN-222(Fe) (PPTP) MEPCMs can not only absorb solar energy for heat storage, but the heterojunction hybrid shell can

also achieve efficient separation of hole-electron pairs to improve the photocatalysis of CO_2 into CO and CH_4 . The current work aims to develop a novel manufacturing technique for the MEPCMs and investigate their solar thermal storage capacity and photocatalytic CO_2 reduction properties.



Scheme 1. Illustration of the fabrication of paraffin@PANI/TiO₂/PCN-222(Fe) MEPCMs by Pickering emulsion polymerization.

2. Results and Discussion

2.1. Morphology Structure of PPTP MEPCMs

Figure 1a,b exhibit the SEM images of KH-570 modified TiO₂ and PCN-222(Fe) NPs, respectively. The particle size of KH-570 modified TiO₂ was about 30 nm. The particle size of PCN-222(Fe) NPs was around 50 nm, and their morphology was regular and generally in a fusiform shape. Figure 1c–g exhibit SEM images of PPTP-1 to PPTP-5, in which a series of MEPCMs with apparent spherical structure can be observed, where the diameter of MEPCMs increased with the decrease of the addition of TiO₂ and PCN-222(Fe) NPs, and the MEPCMs size distribution is between 1 and 8 μm. Furthermore, the amount of TiO₂ and PCN-222(Fe) NPs embedded on the surface of the MEPCM decreased with the continuous increase of the amount of PANI, resulting in the poor dispersion and aggregation of MEPCMs. Moreover, with the decrease of PCN-222(Fe), the size of MEPCMs accordingly decreased. Among them, PPTP-3 MEPCM has an ideal dispersion (Figure 1e), where more NPs are accumulated on the surface. The core-shell structure of PPTP-3 can be observed in the TEM image (Figure 1h), where the TiO₂ and PCN-222(Fe) NPs embedded on the surface can also be observed. Figure 1i is the SEM image of PPTP-3 at the acceleration voltage of 10 kV, and the EDX elemental mappings of PPTP-3 show that C, N, Ti, O, Fe, and Zr elements are dispersed on the surface of MEPCMs, indicating that TiO₂ and PCN-222(Fe) NPs are uniformly embedded on the PANI shell. The above results show that the PPTP MEPCMs with paraffin as the core and PANI/TiO₂/PCN-222(Fe) as the hybrid shell have been successfully prepared.

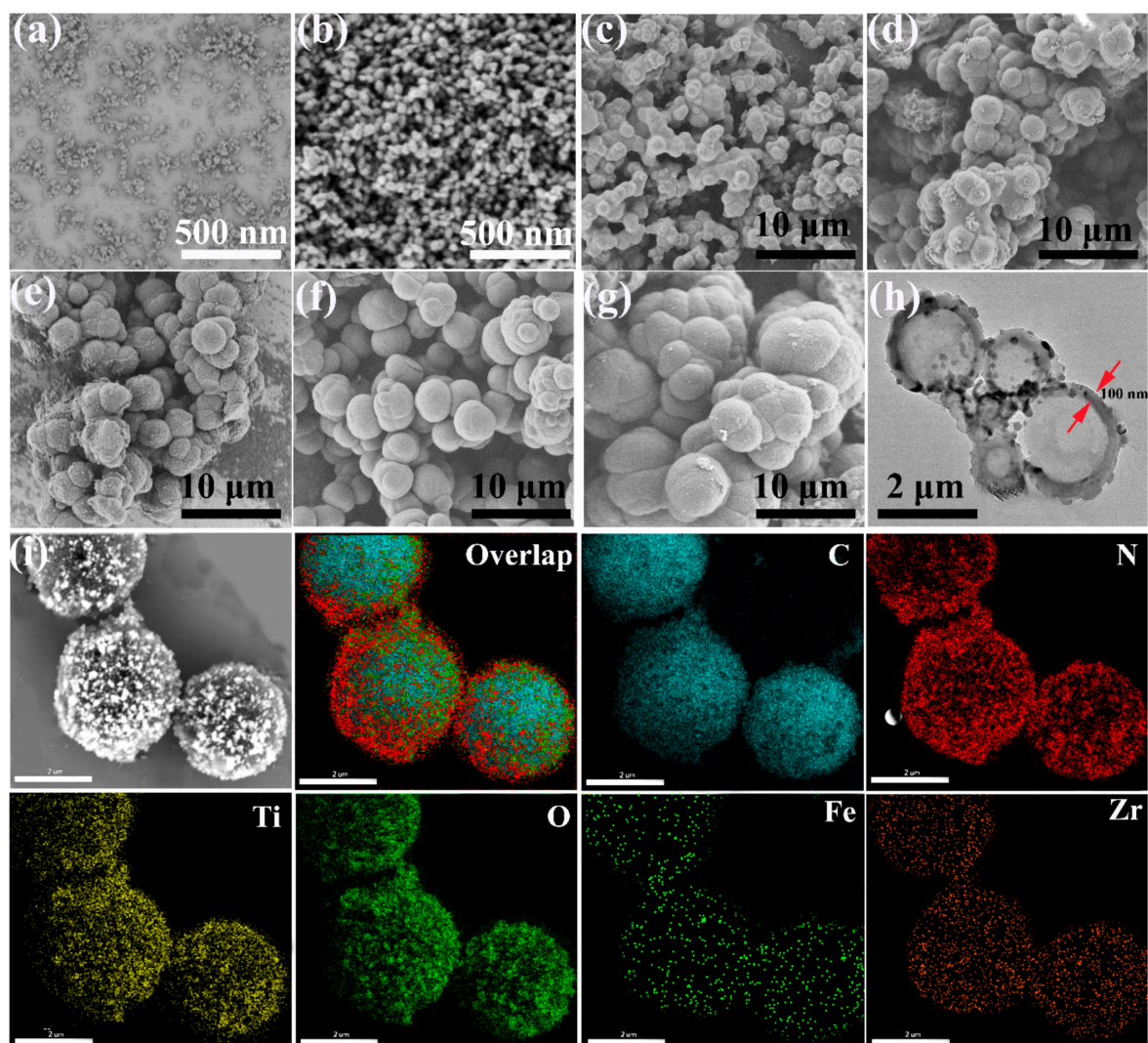


Figure 1. SEM images of (a) P25 NPs, (b) PCN-222(Fe) NPs, and (c–g) PPTP-1 to PPTP-5 MEPCMs. (h) TEM image of PPTP-3. (i) SEM images (CBS detector at 10 kV) of PPTP-3 and the corresponding EDX elemental mappings of overall, C, N, Ti, O, Fe, and Zr (all the plotting scales are two μm).

2.2. Chemical Composition Characterization

FT-IR spectra of TiO_2 , KH-570 modified TiO_2 , paraffin, PANI, and PPTP MEPCMs are shown in Figure 2a. For the TiO_2 , the broad peaks at around 560 and 3400 cm^{-1} are attributed to the Ti-O and hydroxyl groups stretching vibrations, respectively. The peaks of modified TiO_2 at 1633 and 1714 cm^{-1} are attributed to C=C and C=O vibrations of KH-570, indicating the successful modification of TiO_2 by KH-570. The peaks of paraffin at 2917 and 2852 cm^{-1} correspond to the asymmetric stretching vibration and symmetric stretching vibration of $-\text{CH}_2$. The peak at 1471 cm^{-1} is attributed to $-\text{CH}_2$ bending vibration, and the peak at 718 cm^{-1} is assigned to the in-plane rocking vibration of the alkyl chain. In the spectrum of PANI, the peaks at 1564 and 1471 cm^{-1} correspond to C=N and C=C stretching mode of quinone and benzene units, respectively, 1294 cm^{-1} is indexed with C-N stretching mode for benzene ring. For the spectrum of PCN-222(Fe), the symmetric Fe-N stretching at 998 cm^{-1} appears, indicating the successful complexation of Fe with porphyrin ring. In the spectrum of the PPTP-3, the characteristic peaks of the different components can be detected, suggesting that the as-prepared MEPCM consists of paraffin, TiO_2 , PANI, and PCN-222(Fe).

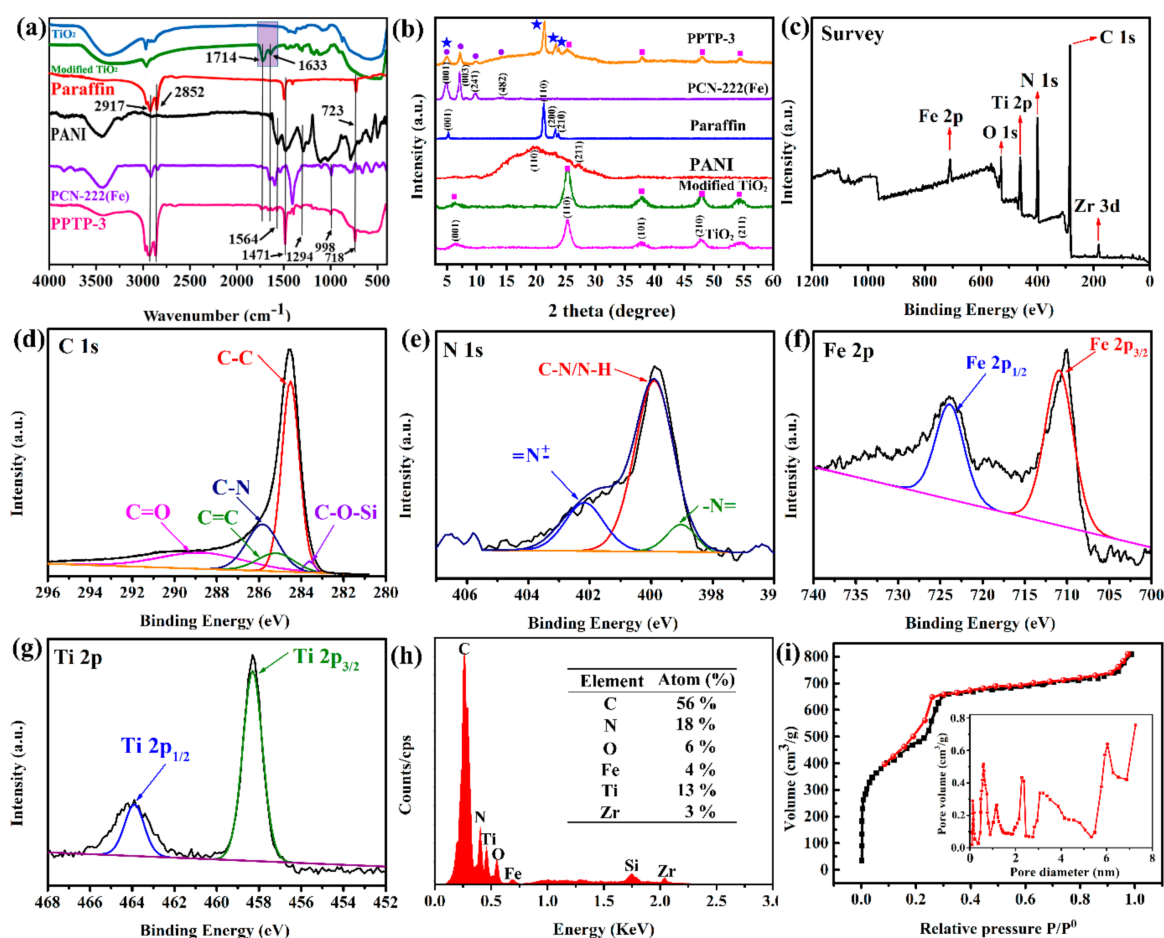


Figure 2. (a) FT-IR spectra and (b) XRD patterns of TiO₂, KH-570 modified TiO₂, paraffin, PANI, PCN-222(Fe), and PPTP-3. XPS spectra of PPTP-3: (c) survey scan, (d) C 1s, (e) N 1s, (f) Fe 2p, and (g) Ti 2p. (h) EDX spectrum and element content (inset) of PPTP-3. (i) N₂ adsorption–desorption isotherms and the corresponding pore-size distributions (inset) of PPTP-3.

The crystal structures of the PPTP-3 and its various components were analyzed by XRD (Figure 2b). The crystal structures and the position of diffraction peaks hardly change after TiO₂ modification, indicating that KH-570 grafting on the TiO₂ surface can not affect its crystallinity. Furthermore, the characteristic diffraction peaks at 2θ of TiO₂ are located at 25.3, 27.5, 48.1, and 54.8°, respectively. The corresponding crystal planes are (110), (101), (210), and (211), showing that TiO₂ NPs is a crystal morphology composed of rutile and anatase mixed-phase (JCPDS No. 21-1272 and JCPDS No. 21-1276) [43]. The wide diffraction angle 2θ of PANI is around 18.4°, which is a unique characteristic diffraction peak of polymer materials [44]. Paraffin diffraction peaks at 2θ are 6.1, 21.2, 22.8, and 23.5°, which corresponds to the (001), (100), (200), and (210) crystal planes (JCPDS No. 40-1995) [45]. The diffraction peaks at $2\theta = 4.8^\circ, 7.1^\circ, 9.8^\circ, 14.4^\circ$ and 19.6° match (001), (003), (241), (161), and (482) crystal planes of PCN-222(Fe) [46]. All the diffraction peaks can be observed in the spectrum of PPTP-3, which also proves that PPTP MEPCMs are composed of paraffin, PANI, TiO₂, and PCN-222(Fe).

Furthermore, the elemental distribution and chemical states of PPTP-3 were characterized by XPS measurement, where the survey XPS spectra confirm the elements of C, N, Fe, O, and Ti in the PPTP-3 (Figure 2c). Four kinds of carbon species were detected in the high-resolution C 1s spectrum of PPTP-3 (Figure 2d): C=C (284.6 eV), C-N (286.1 eV), C-O-Si (283.6 eV), and C=O (288.3 eV). The high-resolution N 1s spectrum was deconvoluted into three nitrogen species (Figure 2e); the peaks at 398.1 and 399 eV are the =N- and C-N/N-H bonds of porphyrin rings in PCN-222(Fe) and PANI molecular chains, respectively.

The peak at 402.4 eV is the protonated amine of PANI molecular chains [47]. The high-resolution Fe 2p spectrum was fitted into two characteristic Fe species at 710.7 (Fe 2p_{3/2}) and 724.5 eV (Fe 2p_{1/2}) (Figure 1f), indicating the introduction of the Fe component into the MOF nanocrystal [48]. In the high-resolution Ti 2p spectrum, signals allocated to Ti 2p_{1/2} and Ti 2p_{3/2} are observed at 463.5 and 457.9 eV (Figure 1g), which indicates the existence of Ti in a tetravalent form [49]. The XPS analysis shows the stable compound states of C, N, Fe, and Ti in the PPTP-3. In addition, the EDX spectrum of PPTP-3 is shown in Figure 2h, the contents of C, N, O, Fe, Ti, and Zr are 56, 18, 6, 4, 13, and 3 atom%, respectively, which also indicates the PPTP MEPCMs with paraffin as core and PANI/TiO₂/PCN-222(Fe) as hybrid shell are successfully fabricated. The above results show that the MEPCMs with paraffin as the core and PANI/TiO₂/PPTP-222(Fe) as the hybrid shell have been successfully prepared.

2.3. Pore Structure and Specific Surface Area Analysis

The pore structure and specific surface area of photocatalysts have an essential impact on the performance, and these parameters of materials were analyzed by the BET analyzer. The pore size of PPTP-3 was calculated according to the BET method, which was mainly concentrated at approximately 1.3, 3.2, and 3.8 nm, respectively (illustration in Figure 2i). These pore sizes match the pore sizes in PANI and PCN-222(Fe) (Figure S1), and the other larger mesopores may result from the piled pores among the MEPCM [50]. According to IUPAC classification, the N₂ adsorption–desorption isotherm belongs to type IV, and a small amount of N₂ adsorption appears under low relative pressure, indicating the existence of micropores. A wide H1 type hysteresis ring appears in the medium pressure region, which proves the existence of mesopores. The BET specific surface area and pore volume of PPTP-3 were 583 m²/g and 0.628 cm³/g, respectively, which well inherits the pore structure of PCN-222(Fe) and PANI.

2.4. Phase Change and Thermal Properties Analysis

The phase change characteristics and thermal properties of pure paraffin and PPTP MEPCMs were analyzed by DSC (Figure 3a). The curves include three solid–liquid phase change peaks in the endothermic stage and three corresponding liquid–solid phase change peaks in the exothermic stage. All the PPTP MEPCMs have similar phase change behavior compared with paraffin. Still, the melting peak temperature T_m decreases slightly, and the crystallization peak temperature T_c increases marginally due to the crystallization confinement of paraffin microencapsulated in the inner space of the hybrid shell [51]. The T_c and T_m of high melting point paraffin used in this work are 50.3 and 45.1 °C, the corresponding crystallization enthalpy ΔH_c and melting enthalpy ΔH_m are 226.3 J·g⁻¹ and 228.5 J·g⁻¹, respectively. A series of PPTP MEPCMs showed excellent encapsulation efficiency E_{en} except for PPTP-1, the E_{en} of PPTP-2 to PPTP-5 MEPCMs is close to 80% and had good heat storage performance (Table 1). The values of encapsulation efficiency (E_{en}), energy storage efficiency (E_{es}), and thermal storage capability (C_{es}) were calculated according to Equations (S1)–(S3) in the Supporting Information. The thermal stability of PPTP-3 was verified by 500 heating–cooling cycles experiments. In Figure 3b, the enthalpy of PPTP-3 hardly decreases after 500 cycles, indicating that as-fabricated MEPCMs have superior thermal stability. Furthermore, the thermal stability of the materials was tested by TGA (Figure 3c,d). The results show that the PANI/TiO₂/PCN-222(Fe) hybrid shell has a good protective effect on paraffin and improves its thermal stability. Significantly, the weight loss of modified P25 was attributed to the removal of KH-570 grafted on the surface of P25 during the temperature of 200–450 °C. PPTP-3 was tested for 500 high–low temperature cycles in the temperature range of 10–60 °C. As shown in Figure 3e, after the high–low temperature cycles test, no liquid paraffin remained on the filter paper, proving that PANI/TiO₂/PCN-222(Fe) hybrid shell can prevent the internal melting core PCM from leaking.

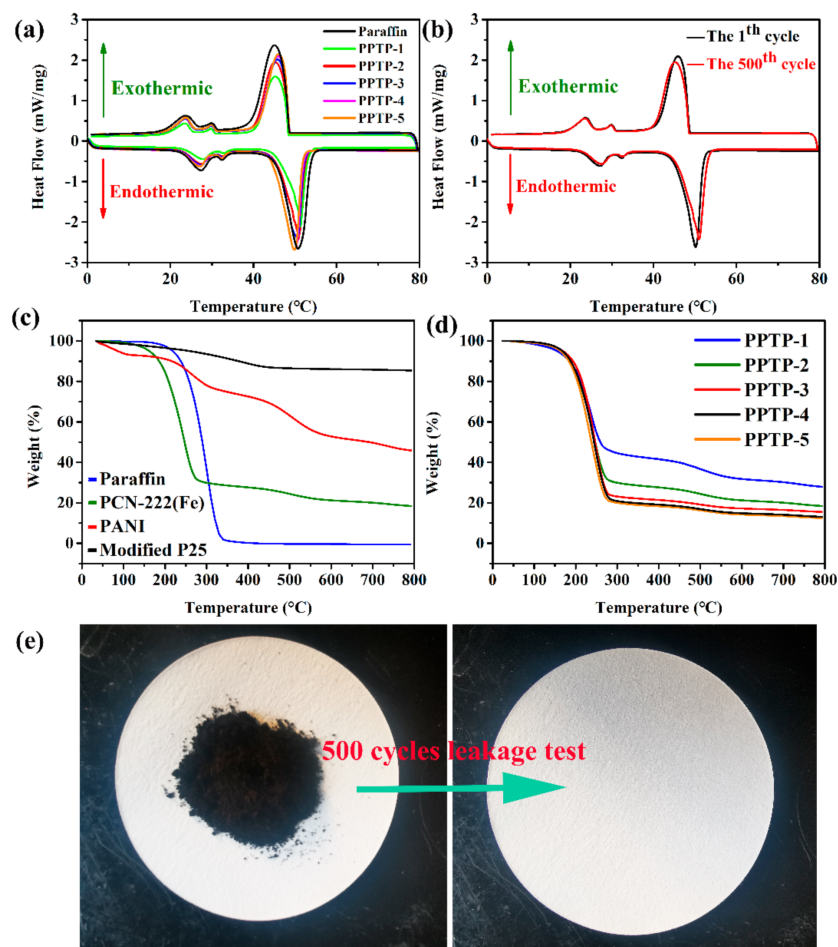


Figure 3. DSC curves of (a) paraffin and PPTP MEPCMs, and (b) 500 high–low temperature cycles of PPTP-3. TGA thermograms of (c) paraffin, PCN-222(Fe), PANI, KH-570 modified TiO₂, and (d) PPTP MEPCMs. (e) Photos of PPTP-3 MEPCM after 500 heating-cooling cycle leaking tests.

Table 1. Thermal property data and the corresponding encapsulation parameters of various samples.

Names	Melting Process		Crystallization Process		ΔT (°C)	Encapsulation Parameters		
	T_m (°C)	ΔH_m (J·g ⁻¹)	T_c (°C)	ΔH_c (J·g ⁻¹)		E_{en} (%)	E_{es} (%)	C_{es} (%)
Paraffin	50.3	226.3	45.1	228.5	5.2	-	-	-
PPTP-1	52.2	138.9	45.3	139.6	6.9	61.4	61.2	99.73
PPTP-2	51.8	164.1	45.7	164.9	6.1	72.5	72.3	99.78
PPTP-3	51.4	167.7	46.2	168.8	5.2	74.1	74.0	99.85
PPTP-4	50.8	172.7	46.4	174.1	4.4	76.3	76.3	99.94
PPTP-5	50.6	174.7	46.4	176.2	4.2	77.2	77.2	99.94

2.5. Photothermal Conversion Performance

To investigate the photothermal absorption-release properties of the materials, a 300 W Xenon lamp ($\lambda > 300$ nm) was used to irradiate paraffin, PCN-222(Fe)/PANI/TiO₂ mixture (the composition ratio is the same as the shell of PPTP-3), and PPTP-3 at the same time and the surface temperature was recorded every 30 s by an infrared thermal imager (Figure 4). In the process of light irradiation and removal, it can be observed that there is an apparent difference in the surface temperature. In Figure 4a, in the course of the light irradiation, the temperature of the PCN-222(Fe)/PANI/TiO₂ mixture continues to rise rapidly within 150 s, and the maximum temperature reaches about 85 °C. In contrast, the temperature rise speed of PPTP-3 is slightly slower than that of the mixture due to

the heat absorption of internal paraffin; the maximum temperature within 150 s reaches about 49 °C. Meanwhile, the ascending speed of paraffin surface temperature is the slowest, and there is a distinct temperature hysteresis due to the poor photothermal conversion capability. In the cooling process after removing the light source (Figure 4b), in contrast to the fastest decrease of the temperature of the PCN-222(Fe)/PANI/TiO₂ mixture, the temperature of PPTP-3 dropped slower but faster than that of paraffin. Furthermore, to observe the temperature variation, the temperature response curves of samples over time were collected (Figure 4c). During the light radiation stage, the temperature of the PCN-222(Fe)/PANI/TiO₂ mixture almost linearly and rapidly increases to 78.5 °C in 75 s because of the ultra-high thermal conductivity of the mixture without paraffin. Nevertheless, for paraffin and PPTP-3 MEPCM, the temperatures rise rate are slow and increased to 24.8 and 44.6 °C after 160 s, respectively. After removing the irradiation light source, the temperature of the PCN-222(Fe)/PANI/TiO₂ mixture quickly decreases from 78.5 to 12 °C within 100 s because of the high thermal conductivity of the hybrid shell. Meanwhile, the surface temperature of PPTP-3 and paraffin drops to 12 °C after cooling for respectively 120 s and 180 s due to the thermal insulation of the inner paraffin. The above results show that PCN-222(Fe)/PANI/TiO₂ shell has superior photothermal conversion capacity than paraffin, and PPTP-3 integrates the photothermal conversion and heat energy storage, which significantly improves the thermal response and thermal regulation performance of PPTP-3.

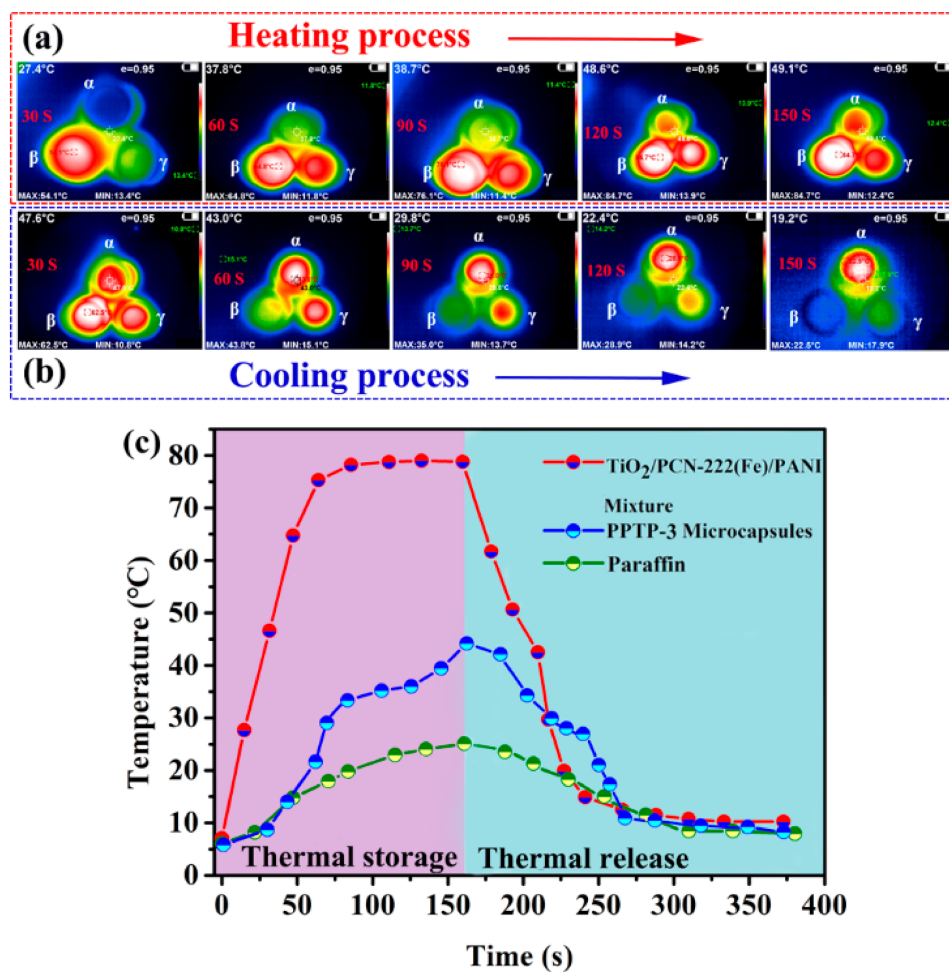


Figure 4. Infrared thermography images of α : paraffin, β : TiO₂/PCN-222(Fe)/PANI mixture, and γ : PPTP-3 during the (a) light radiation stage and (b) after removing the light radiation stage. (c) Temperature response curves of samples over time.

2.6. Photoelectric Performance

To investigate the photoelectrochemical characteristics of PPTP MEPCMs, TiO_2 , PCN-222(Fe), PANI, $\text{TiO}_2/\text{PCN-222(Fe)}/\text{PANI}$ ternary mixture, and PPTP MEPCMs were characterized by employing electrochemical workstation. The transferability of photogenerated electrons was analyzed by observing the photocurrent-time ($I-t$) and the EIS Nyquist plot changes. The evolution of $I-t$ was inversely proportional to that of the EIS Nyquist plot (Figure 5). The $I-t$ curves are shown in Figure 5a, the photocurrent intensity of the PPTP-1 to PPTP-5 MEPCMs is better than that of TiO_2 , PCN-222(Fe), PANI, and the ternary mixture. Furthermore, with the mass ratio of PCN-222(Fe)/PANI in the MEPCMs increasing first and then decreasing, the photocurrent intensity of PPTP-1 to PPTP-5 MEPCMs also increases first and then decreases, and in which the photocurrent intensity of PPTP-3 reaches the highest due to the maximum mass fraction of PCN-222(Fe) in the MEPCM. It can be observed that the EIS curves are similar to arc shape (Figure 5b), where the radius represents the impedance value. The EIS curves show that the impedance of PPTP-3 is the smallest, indicating the optimal photoelectron–hole pair separation efficiency because of the suitable heterojunction composition ratio. In brief, the PPTP-3 ternary hybrid shell can effectively enhance the separation efficiency of electron–hole pairs in the catalyst and then improve the photocatalytic reduction capacity.

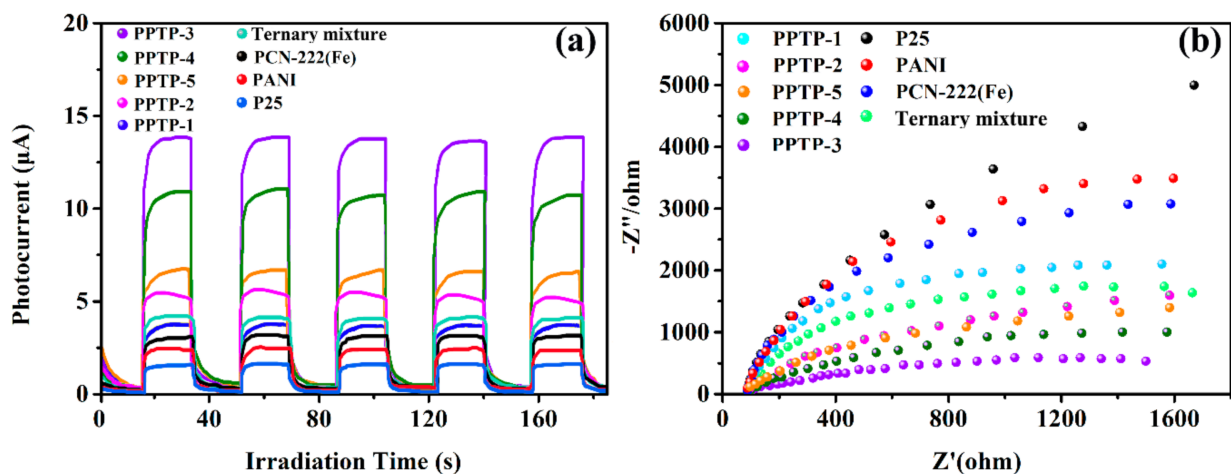


Figure 5. (a) Photocurrent-time ($I-t$) curves and (b) EIS plots of TiO_2 , PCN-222(Fe), PANI, $\text{TiO}_2/\text{PCN-222(Fe)}/\text{PANI}$ ternary mixture, and PPTP MEPCMs.

For demonstrating the influence of heterojunction of MEPCMs shell on optical properties of composite materials, UV-Vis diffuse reflectance spectra (DRS) were further employed to investigate the light-absorbing ability (Figure 6a). Compared with pure TiO_2 P25, pure PANI and PCN-222(Fe) have strong light absorption in the natural light region, $\text{TiO}_2/\text{PCN-222(Fe)}/\text{PANI}$ mixture, and PPTP-3 with ternary heterojunction have also been well inherited in light absorption ability. To clarify the effect of coupling on bandgap (E_g), the E_g of various samples were calculated based on the Kubelka–Munk equation: $\alpha h\nu = k(h\nu - E_g)n/2$ and $(\alpha h\nu)^{n/2} - h\nu$ curves (Figure 6b), where TiO_2 is an indirect semiconductor, $n = 4$; PCN-222(Fe) and PANI are direct semiconductors, $n = 1$ [52]. Thus, the E_g of TiO_2 , PCN-222(Fe), and PANI are 3.1, 1.63, and 2.1 eV, respectively. Moreover, the E_g of the ternary mixture PCN-222(Fe)/PANI/ TiO_2 and PPTP-3 are 1.91 and 1.82 eV, respectively, indicating the integration of ternary heterojunction has more influence than the simple mixture.

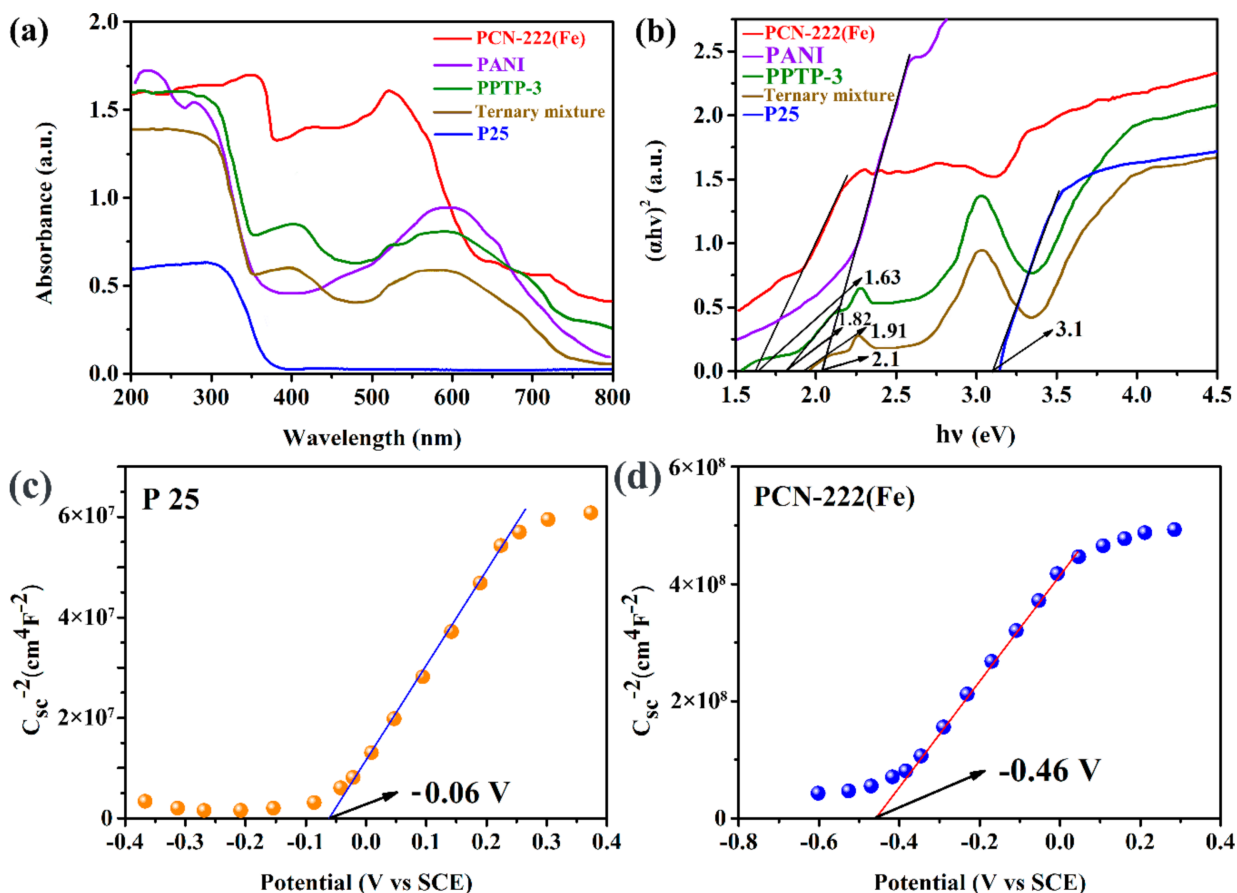


Figure 6. (a) UV-Vis diffuse reflectance spectra (UV-Vis DRS) and (b) band gap (E_g) plots. Mott-Schottky plots of (c) TiO_2 (P25) and (d) PCN-222(Fe).

To obtain the bandgap structure of each material, the flat band potentials (E_{FB}) of TiO_2 and PCN-222(Fe) were calculated by Mott-Schottky plots. The tangent slopes of Mott-Schottky curves on TiO_2 and PCN-222(Fe) are positive, indicating that they are n-type semiconductors (Figure 6c,d). It can be seen from the Mott-Schottky plots that the E_{FB} of TiO_2 and PCN-222(Fe) are -0.06 and -0.46 V vs. Ag/AgCl, respectively. Based on Yuan's research [53], the E_{CB} potential of n-type semiconductors is 0.2 V higher than E_{FB} . Therefore, the E_{CB} values of TiO_2 and PCN-222(Fe) are -0.26 V and -0.66 V, according to the formula $E_g = E_{\text{VB}} - E_{\text{CB}}$; thus, the valence band potential (E_{VB}) of TiO_2 and PCN-222(Fe) is 2.84 V and 0.97 V, respectively. The above data provide theoretical support for the subsequent catalytic mechanism.

2.7. Photocatalytic Performance of Catalysts for CO_2 Photoreduction

The results of CO_2 photoreduction catalyzed by various photocatalysts are shown in Figure 7a, where the main product is CO with a small amount of CH_4 . The reduction rate of CO_2 into CO catalyzed by PANI, TiO_2 , and PCN-222(Fe) are 4.12, 0.73, and 8.4 $\mu\text{mol g}^{-1} \text{h}^{-1}$, respectively. The reduction rate of CO_2 into CO over PPTP-1 to PPTP-5 first increases and then decreases. The PPTP-3 reaches the optimal value of 45.16 $\mu\text{mol g}^{-1} \text{h}^{-1}$, which is mainly due to the highest mass fraction of PCN-222(Fe) in PPTP-3 causing the optimal photocurrent density, hole-electron separation efficiency, and suitable energy band. As the optimal photocatalyst, PPTP-3 has the highest CO yield, which is 11, 5.4, and 62 times higher than that of PANI, PCN-222(Fe), and TiO_2 , respectively. Moreover, the selectivity of CO catalyzed by PPTP MEPCMs is relatively high, where the selectivity of CO over PPTP MEPCMs is almost higher than 96%. To verify the photocatalytic specificity of heterojunction of PPTP-3, the ternary mixture (PCN-222(Fe)/PANI/ TiO_2) was also adopted to carry out

the CO₂ photoreduction, where the reduction rate of CO₂ into CO is 20.23 $\mu\text{mol g}^{-1} \text{h}^{-1}$ with the CH₄ reduction rate of 3.25 $\mu\text{mol g}^{-1} \text{h}^{-1}$, indicating the heterojunction of PPTP-3 shell has better catalytic performance because of the more favorable light absorption of the heterojunction catalyst and the weaker recombination of charges and holes between the three components.

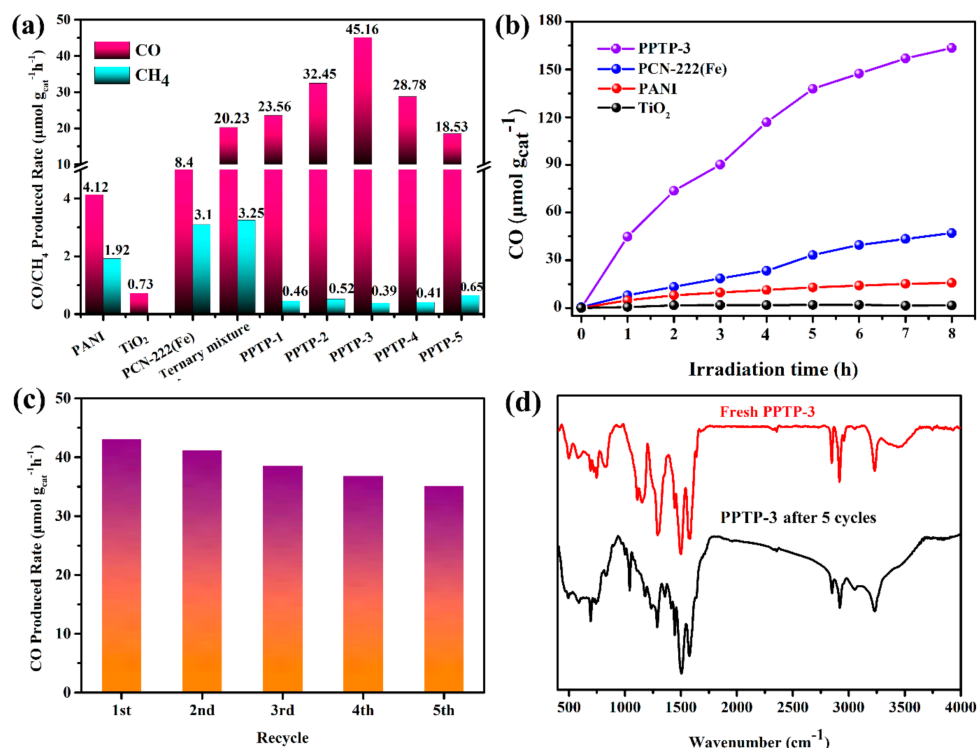


Figure 7. (a) CO and CH₄ produced rate by PCN-222(Fe), TiO₂, PANI, and PPTP-1 to PPTP-5 under 300 W Xe lamps. (b) CO reduction yield by PCN-222(Fe), TiO₂, PANI, and PPTP-3 within 8 h. (c) CO produced rate after 5 times cycling utilization of PPTP-3. (d) FTIR spectra of PPTP-3 before and after 5 times cycling photocatalysis.

The results of total CO evolution yield by PCN-222(Fe), TiO₂, PANI, and PPTP-3 with Xe lamp within 8 h are shown in Figure 7b. In the process of photoreduction within 8 h, although the reduction rate of CO₂ catalyzed by PPTP-3 decreased slightly after 3 h, the evolution rate of CO was still maintained at a comparatively high level. The evolution amount of CO catalyzed by PPTP-3 is much higher than that of the other three single components, indicating that the ideal activity of PPTP-3 remains during the long-term catalytic process. In addition, the catalytic stability of PPTP-3 was further verified by cycle experiments (Figure 7c). After five cycles of 1 h, the CO produced rate did not decay significantly, and there was still a 90% CO produced rate compared with the first cycle. The structural stability of PPTP-3 after five cycles was verified by FTIR spectra. It can be seen from Figure 7d that the functional groups in the FTIR spectra of PPTP-3 before and after the cycles remained well.

2.8. Photocatalysis Mechanism of PPTP-3 MEPCM for CO₂ Photoreduction

The mechanism of CO₂ photoreduction catalyzed by PPTP-3 MEPCM is shown in Figure 8. In the hybrid shell of PPTP-3, PCN-222(Fe) and TiO₂ NPs are dispersedly embedded on the conductive polymer PANI. PANI, as a p-type conductive polymer, can absorb natural light and further induce π - π^* transition. Then, the excited state electrons transfer from the highest occupied molecular orbital (HOMO) to the lowest unoccupied molecular orbital (LUMO). The potentials of the excited state electrons on the LUMO and HOMO orbitals are 0.5 and -1.6 eV, respectively, and E_g is 2.1 eV [54], which matches the bandgap

parameters of PANI in this work. Based on the above analysis of the bandgap structures of PCN-222(Fe), TiO₂, and PANI, a ternary heterojunction of PCN-222(Fe)/TiO₂/PANI was proposed. From the potential values of the three components, it can be seen that PCN-222(Fe) and TiO₂ have an excellent potential match with PANI, and then an internal electric field was established. Under the irradiation of natural light, quantities of photogenerated electrons accumulated on the LUMO of PANI, and then the electrons were quickly transferred to the conduction band (CB) PCN-222(Fe). The standard potential (−0.33 V vs. NHE) of O₂/[•]O₂ is more negative than the CB of TiO₂ (−0.26 eV), in which the [•]O₂[−] cannot generate in thermodynamics. Therefore, the electrons on the CB of TiO₂ will continue to migrate to the HOMO of PANI. As such, VB of PCN-222(Fe) (0.97 eV) and HOMO potential of PANI (0.5 eV) are more negative than H₂O/[•]OH (1.99 V vs. NHE) or OH[−]/[•]OH (2.34 V vs. NHE), which also prohibits the generation of [•]OH. Therefore, in the process of illumination, the CB values of reduction potentials E^0 (CO₂/CO, 0.53 V vs. NHE) and E^0 (CO₂/CH₄, 0.24 V vs. NHE) are more positive than the CB value of PCN-222(Fe) (−0.66 V vs. NHE). Most of the electrons of CB on PCN-222(Fe) were used to reduce CO₂, to maintain the strong reducibility of CB belonging to PCN-222(Fe). MOFs tend to produce H₂O₂ during the photoreduction reaction. Accordingly, excessive H₂O₂ will consume photoinduced electrons and further weaken the reduction ability of the substrate. By compounding with other materials, such as TiO₂ or PANI, the generation of H₂O₂ can be effectively reduced, thus improving the photoreduction performance. When exposed to light, photogenerated holes (H⁺) of PPTP-3 MEPCM can be produced simultaneously. Since the HOMO potential (0.5 V vs. NHE) of PANI is more negative than the VB of PCN-222(Fe), the photogenerated H⁺ on the VB of PCN-222(Fe) will transfer to the HOMO of PANI. The oxidation potential E^0 (O₂/H₂O, 0.82 V vs. NHE) is more VB potential of TiO₂ is more negative than the HOMO potential of PANI. Hence, H₂O will be oxidized to O₂ and [•]OH on the VB of TiO₂. In PCN-222(Fe)/TiO₂/PANI ternary heterojunction, PANI can not only increase the concentration of photogenerated electrons on CB of PCN-222(Fe) but also absorb the photogenerated H⁺ of PCN-222(Fe) and TiO₂, reducing the recombination of electrons and H⁺ in PCN-222(Fe) and TiO₂. Thus, according to Equations (1)–(3) [55], the reduction of CO₂ and oxidation of H₂O will proceed successfully.

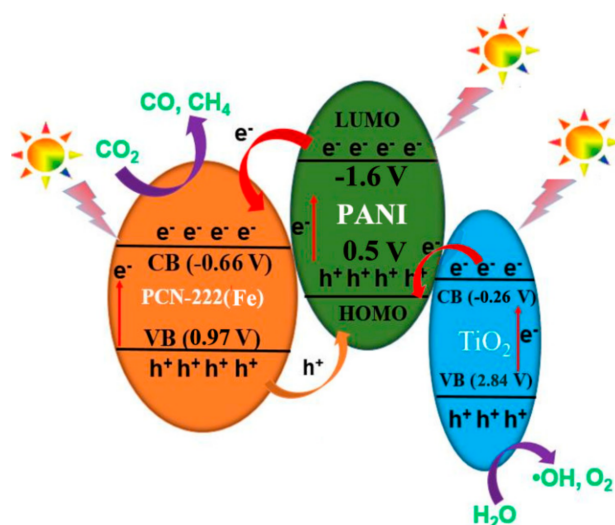


Figure 8. Mechanism of CO₂ photoreduction over PPTP-3 MEPCM.

2.9. Performance Comparison of MEPCMs with Organic–Inorganic Hybrid Shells in the Literature

Preparation conditions and key parameters are important references to evaluate the comprehensive performance of MEPCMs microcapsules with organic–inorganic hybrid shells. First, the emulsion process requires additional co-emulsifiers in most literature (Table S2). In this work, only the Pickering stabilizers were added without co-emulsifiers in the preparation of microcapsules, making the preparation process green and environmentally friendly. The ΔH_m and E_{en} of as-prepared microcapsules in this work are ideal under the condition that no co-emulsifier was added, especially ΔH_m basically achieves the highest value. The thermal stability of microcapsules was verified by 500 heating–cooling cycles, in which the enthalpy of microcapsules hardly decreases after 500 cycles. Few MEPCMs microcapsules with organic–inorganic hybrid shells have additional functions other than TES, but the integration of TES and CO₂ photoreduction has not been seen before in the literature. Therefore, performance comparison of PPTP-3 with ternary heterojunction photocatalysts in the literature is listed in Table S3. The evolution rate of CO catalyzed by PPTP-3 exceeds most of the recently reported ternary heterojunction photocatalysts, further indicating the ternary heterojunction of the PPTP-3 shell has the superior structural advantage and light utilization efficiency.

3. Conclusions

In summary, we have fabricated a novel type of bi-functional paraffin@PANI/TiO₂/PCN-222(Fe) MEPCMs with thermal energy storage and CO₂ photoreduction ability by Pickering emulsion polymerization. The PPTP MEPCMs are composed of paraffin as PCM core and PANI/TiO₂/PCN-222(Fe) as hybrid shell, in which the ternary heterojunction was also constructed on the shell owing to the tight contact of the three components. The MEPCMs realized the optimal phase change enthalpy of 174.7 J·g⁻¹ with an encapsulation efficiency of 77.2%. The thermal properties, chemical composition, and morphological structure were retained well after 500 high–low temperature cycles test. Under natural light irradiation, the photoreduction of CO₂ into CO and CH₄ by the MEPCMs showed excellent activity because of the suitable band gap and enhanced separation of the photogenerated electron–hole pair. The results CO evolution rate was 45.16 μmol g⁻¹ h⁻¹, which is 5.4, 11, and 62 times higher than pure PCN-222(Fe), PANI, and TiO₂, respectively. The CO evolution rate could maintain basically after five cycles of CO₂ photoreduction within 1 h, and there was still 90% of CO yield compared with the initial test. The as-fabricated bi-functional MEPCMs will show potential applications in the energy-saving building materials and construction of photocatalytic systems due to the solar energy storage and CO₂ photoreduction.

Supplementary Materials: The following are available online at <https://www.mdpi.com/article/10.3390/nano12010002/s1>, Figure S1: N₂ adsorption-desorption isotherms and the corresponding pore-size distributions (inset) of PCN-222(Fe) NPs, Table S1: Preparation recipes for PPTP MEPCMs, Table S2: Performance comparison of microencapsulated PCMs with organic-inorganic hybrid shell in the literature, Table S3: Performance comparison of ternary heterojunction photocatalysts in the literature, Equations (S1)–(S3), Experimental: Chemicals, Surface modification of TiO₂ NPs, Ligand Synthesis Procedures, Synthesis of PCN-222(Fe) NPs, Fabrication of paraffin@PANI/TiO₂/PCN-222(Fe) (PPTP) MEPCMs, Characterization, Electrochemical test, Photocatalytic reaction of CO₂; Calculation formula of E_{en} , E_{es} , and C_{es} . References [56–80] are cited in the Supplementary Materials.

Author Contributions: Methodology and experimental design: W.S. and Y.H.; resources: X.Z.; supervision: X.Z.; writing—original draft: W.S.; writing—review and editing: X.Z. All authors have read and agreed to the published version of the manuscript.

Funding: This work was supported by grants from the National Natural Science Foundation of China (Grant No. 51573038), the Natural Science Foundation of Hebei Province (No. E2020202146 and E2020202133), and Hebei Key Research and Development Program (No. 21371401D).

Institutional Review Board Statement: Not applicable.

Informed Consent Statement: Not applicable.

Data Availability Statement: The data presented in this study are available on request from the corresponding author.

Conflicts of Interest: The authors declare no competing financial interest.

References

1. Chilvers, J.; Bellamy, R.; Pallett, H.; Hargreaves, T. A systemic approach to mapping participation with low-carbon energy transitions. *Nat. Energy* **2021**, *6*, 250–259. [[CrossRef](#)]
2. Weck, P.F.; Kim, E. Solar Energy storage in phase change materials: First-principles thermodynamic modeling of magnesium chloride hydrates. *J. Phys. Chem. C* **2014**, *118*, 4618–4625. [[CrossRef](#)]
3. Liu, H.; Wang, X.; Wu, D. Innovative design of microencapsulated phase change materials for thermal energy storage and versatile applications: A review. *Sustain. Energy Fuels* **2019**, *3*, 1091–1149. [[CrossRef](#)]
4. Bazri, S.; Badruddin, I.A.; Naghavi, M.S.; Bahiraei, M. A review of numerical studies on solar collectors integrated with latent heat storage systems employing fins or nanoparticles. *Renew. Energy* **2018**, *118*, 761–778. [[CrossRef](#)]
5. Akhiani, A.R.; Mehrali, M.; Latibari, S.T.; Mehrali, M.; Mahlia, T.M.I.; Sadeghinezhad, E.; Metselaar, H.S.C. One-step preparation of form-stable phase change material through self-assembly of fatty acid and graphene. *J. Phys. Chem. C* **2015**, *119*, 22787–22796. [[CrossRef](#)]
6. Lu, Y.; Xiao, X.; Liu, Y.; Wang, J.; Qi, S.; Huan, C.; Liu, H.; Zhu, Y.; Xu, G. Achieving multifunctional smart textile with long afterglow and thermo-regulation via coaxial electrospinning. *J. Alloy. Compd.* **2020**, *812*, 152144. [[CrossRef](#)]
7. Mehrali, M.; Johan, E.; Shahi, M.; Mahmoudi, A. Simultaneous solar-thermal energy harvesting and storage via shape stabilized salt hydrate phase change material. *Chem. Eng. J.* **2021**, *405*, 126624. [[CrossRef](#)]
8. Li, X.; Sun, L.; Sui, H.; He, L.; Yuan, W.; Han, Z. A novel polymeric adsorbent embedded with phase change materials (PCMs) microcapsules: Synthesis and application. *Nanomaterials* **2019**, *9*, 736. [[CrossRef](#)]
9. Woo, H.Y.; Lee, D.W.; Yoon, T.Y.; Kim, J.B.; Chae, J.-Y.; Paik, T. Sub-100-nm nearly monodisperse *n*-paraffin/PMMA phase change nanobeads. *Nanomaterials* **2021**, *11*, 204. [[CrossRef](#)]
10. Kong, L.; Kong, X.; Ji, Z.; Wang, X.; Zhang, X. Large-scale fabrication of a robust superhydrophobic thermal energy storage sprayable coating based on polymer nanotubes. *ACS Appl. Mater. Interfaces* **2020**, *12*, 49694–49704. [[CrossRef](#)]
11. Zeng, J.-L.; Zhu, F.-R.; Yu, S.-B.; Xiao, Z.-L.; Yan, W.-P.; Zheng, S.-H.; Zhang, L.; Sun, L.-X.; Cao, Z. Myristic acid/polyaniline composites as form stable phase change materials for thermal energy storage. *Sol. Energy Mater. Sol. Cells* **2013**, *114*, 136–140. [[CrossRef](#)]
12. Zhu, Y.; Qin, Y.; Wei, C.; Liang, S.; Luo, X.; Wang, J.; Zhang, L. Nanoencapsulated phase change materials with polymer-SiO₂ hybrid shell materials: Compositions, morphologies, and properties. *Energ. Convers. Manag.* **2018**, *164*, 83–92. [[CrossRef](#)]
13. Ji, W.; Cheng, X.; Chen, S.; Wang, X.; Li, Y. Self-assembly fabrication of GO/TiO₂@paraffin microcapsules for enhancement of thermal energy storage. *Powder Technol.* **2021**, *385*, 546–556. [[CrossRef](#)]
14. Jiang, X.; Luo, R.; Peng, F.; Fang, Y.; Akiyama, T.; Wang, S. Synthesis, characterization and thermal properties of paraffin microcapsules modified with nano-Al₂O₃. *Appl. Energy* **2015**, *137*, 731–737. [[CrossRef](#)]
15. Sun, N.; Xiao, Z. Synthesis and performances of phase change materials microcapsules with a Polymer/BN/TiO₂ hybrid shell for thermal energy storage. *Energy Fuels* **2017**, *31*, 10186–10195. [[CrossRef](#)]
16. Wang, X.; Guo, Y.; Su, J.; Zhang, X.; Wang, Y.; Tan, Y. Fabrication and characterization of novel electrothermal self-healing microcapsules with graphene/polymer hybrid shells for bitumenous material. *Nanomaterials* **2018**, *8*, 419. [[CrossRef](#)]
17. Texter, J. Graphene oxide and graphene flakes as stabilizers and dispersing aids. *Curr. Opin. Colloid Interface Sci.* **2015**, *20*, 454–464. [[CrossRef](#)]
18. Yu, Y.; He, L.; Lu, P.; Yuan, Y.; Zhang, H. Preparation, performances and applications of multi-functional photoluminescence form-stable phase change materials. *Polymer* **2020**, *189*, 122211. [[CrossRef](#)]
19. Zhang, X.; Wang, X.; Wu, D. Design and synthesis of multifunctional microencapsulated phase change materials with silver/silica double-layered shell for thermal energy storage, electrical conduction and antimicrobial effectiveness. *Energy* **2016**, *111*, 498–512. [[CrossRef](#)]
20. Daou, I.; El-Kaddadi, L.; Zegaoui, O.; Asbik, M.; Zari, N. Structural, morphological and thermal properties of novel hybrid-microencapsulated phase change materials based on Fe₂O₃, ZnO and TiO₂ nanoparticles for latent heat thermal energy storage applications. *J. Energy Storage* **2018**, *17*, 84–92. [[CrossRef](#)]
21. Zhang, H.; Zou, Y.; Sun, Y.; Sun, L.; Xu, F.; Zhang, J.; Zhou, H. A novel thermal-insulating film incorporating microencapsulated phase-change materials for temperature regulation and nano-TiO₂ for UV-blocking. *Sol. Energ. Mat. Sol. C.* **2015**, *137*, 210–218. [[CrossRef](#)]
22. Wang, H.; Li, Y.; Zhao, L.; Shi, X.; Song, G.; Tang, G. A facile approach to synthesize microencapsulated phase change materials embedded with silver nanoparticle for both thermal energy storage and antimicrobial purpose. *Energy* **2018**, *158*, 1052–1059. [[CrossRef](#)]
23. Hou, P.; Qin, M.; Cui, S.; Zu, K. Preparation and characterization of metal-organic framework /microencapsulated phase change material composites for indoor hygrothermal control. *J. Build. Eng.* **2020**, *31*, 101345. [[CrossRef](#)]

24. Zhao, Y.; Kong, W.; Jin, Z.; Fu, Y.; Wang, W.; Zhang, Y.; Liu, J.; Zhang, B. Storing solar energy within Ag-paraffin@halloysite microspheres as a novel self-heating catalyst. *Appl. Energy* **2018**, *222*, 180–188. [[CrossRef](#)]
25. Zhao, L.; Wang, H.; Luo, J.; Liu, Y.; Song, G. Fabrication and properties of microencapsulated n-octadecane with TiO₂ shell as thermal energy storage materials. *Sol. Energy* **2016**, *127*, 28–35. [[CrossRef](#)]
26. Xu, B.; Zhou, J.; Ni, Z.; Zhang, C.; Lu, C. Synthesis of novel microencapsulated phase change materials with copper and copper oxide for solar energy storage and photo-thermal conversion. *Sol. Energy Mater. Sol. Cells* **2018**, *179*, 87–94. [[CrossRef](#)]
27. Ma, X.; Liu, H.; Chen, C.; Liu, Y.; Zhang, L.; Xu, B.; Xiao, F. Synthesis of novel microencapsulated phase change material with SnO₂/CNTs shell for solar energy storage and photo-thermal conversion. *Mater. Res. Express* **2020**, *7*, 015513. [[CrossRef](#)]
28. Liu, H.; Wang, X.; Wu, D. Tailoring of bifunctional microencapsulated phase change materials with CdS/SiO₂ double-layered shell for solar photocatalysis and solar thermal energy storage. *Appl. Therm. Eng.* **2018**, *134*, 603–614. [[CrossRef](#)]
29. Sun, W.; Wang, X.; Zhang, X.; Kong, X. Design and synthesis of microencapsulated phase-change materials with a poly(divinylbenzene)/dioxide titanium hybrid shell for energy storage and formaldehyde photodegradation. *J. Phys. Chem. C* **2020**, *124*, 20806–20815. [[CrossRef](#)]
30. Cui, W.; He, J.; Wang, H.; Hu, J.; Liu, L.; Liang, Y. Polyaniline hybridization promotes photo-electro-catalytic removal of organic contaminants over 3D network structure of rGH-PANI/TiO₂ hydrogel. *Appl. Catal. B Environ.* **2018**, *232*, 232–245. [[CrossRef](#)]
31. Inoue, T.; Fujishima, A.; Konishi, S.; Honda, K. Photoelectrocatalytic reduction of carbon dioxide in aqueous suspensions of semi-conductor powders. *Nature* **1979**, *277*, 637–638. [[CrossRef](#)]
32. Zheng, Z.; Xu, H.; Xu, Z.; Ge, J. A monodispersed spherical Zr-based metal-organic framework catalyst, Pt/Au@Pd@UIO-66, comprising an Au@Pd core-shell encapsulated in a UIO-66 center and its highly selective CO₂ hydrogenation to produce CO. *Small* **2018**, *14*, 1702812. [[CrossRef](#)]
33. Wang, G.; He, C.-T.; Huang, R.; Mao, J.; Wang, D.; Li, Y. Photoinduction of Cu single atoms decorated on UiO-66-NH₂ for enhanced photocatalytic reduction of CO₂ to liquid fuels. *J. Am. Chem. Soc.* **2020**, *142*, 19339–19345. [[CrossRef](#)]
34. Ostad, M.I.; Shahrak, M.N.; Galli, F. Photocatalytic carbon dioxide reduction to methanol catalyzed by ZnO, Pt, Au, and Cu nanoparticles decorated zeolitic imidazolate framework-8. *J. CO₂ Util.* **2021**, *43*, 101373. [[CrossRef](#)]
35. Jin, J. Porphyrin-based metal–organic framework catalysts for photoreduction of CO₂: Understanding the effect of node connectivity and linker metalation on activity. *New J. Chem.* **2020**, *44*, 15362–15368. [[CrossRef](#)]
36. Duan, S.; Wu, S.; Wang, L.; She, H.; Huang, J.; Wang, Q. Rod-shaped metal organic framework structured PCN-222(Cu)/TiO₂ composites for efficient photocatalytic CO₂ reduction. *Acta Phys. Chim. Sin.* **2020**, *36*, 1905086. [[CrossRef](#)]
37. Jin, J. Highly stable and efficient visible-light-driven carbon dioxide reduction by zirconium–metalloporphyrin PCN-222 via dual catalytic routes. *React. Kinet. Mech. Catal.* **2020**, *131*, 1–12. [[CrossRef](#)]
38. Jiang, Z.; Xu, X.; Ma, Y.; Cho, H.S.; Ding, D.; Wang, C.; Wu, J.; Oleynikov, P.; Jia, M.; Cheng, J.; et al. Filling metal–organic framework mesopores with TiO₂ for CO₂ photoreduction. *Nat. Cell Biol.* **2021**, *586*, 549–554. [[CrossRef](#)]
39. Cheng, X.M.; Gu, Y.; Zhang, X.Y.; Dao, X.Y.; Wang, S.Q.; Ma, J.; Zhao, J.; Sun, W.Y. Crystallographic facet heterojunction of MIL-125-NH₂(Ti) for carbon dioxide photoreduction. *Appl. Catal. B Environ.* **2021**, *298*, 120524. [[CrossRef](#)]
40. Hariri, R.; Saeed, D. Effective visible-light CO₂ photoreduction over (metallo)porphyrin-based metal-organic frameworks to achieve useful hydrocarbons. *Appl. Organomet. Chem.* **2021**, *35*, 6422. [[CrossRef](#)]
41. Xu, H.-Q.; Hu, J.; Wang, D.; Li, Z.; Zhang, Q.; Luo, Y.; Yu, S.-H.; Jiang, H.-L. Visible-light photoreduction of CO₂ in a metal–organic framework: Boosting electron–hole separation via electron trap states. *J. Am. Chem. Soc.* **2015**, *137*, 13440–13443. [[CrossRef](#)] [[PubMed](#)]
42. Pandiselvi, K.; Fang, H.; Huang, X.; Wang, J.; Xu, X.; Li, T. Constructing a novel carbon nitride/polyaniline/ZnO ternary heterostructure with enhanced photocatalytic performance using exfoliated carbon nitride nanosheets as supports. *J. Hazard. Mater.* **2016**, *314*, 67–77. [[CrossRef](#)] [[PubMed](#)]
43. Krishnakumar, B.; Kumar, S.; Gil, J.M.; Pandiyani, V.; Aguiar, A.; Sobral, A.J.N. Highly active P25@Pd/C nanocomposite for the degradation of Naphthol Blue Black with visible light. *J. Mol. Struct.* **2018**, *1153*, 346–352. [[CrossRef](#)]
44. Madaswamy, S.L.; Alfakeer, M.; Bahajjaj, A.A.A.; Ouladsmame, M.; Wabaidur, S.M.; Chen, C.-X.; Dhanusuraman, R. Remarkable electrocatalytic activity of Pd nanoparticles dispersed on polyaniline-polydiphenylamine copolymer nanocomposite for methanol and ethanol oxidation reaction. *Synth. Met.* **2021**, *281*, 116925. [[CrossRef](#)]
45. Zhang, Z.; Liu, Y.; Wang, J.; Sun, L.; Xie, T.; Yang, K.; Li, Z. Preparation and characterization of high efficiency microencapsulated phase change material based on paraffin wax core and SiO₂ shell derived from sodium silicate precursor. *Colloids Surfaces A* **2021**, *625*, 126905. [[CrossRef](#)]
46. Wei, C.; Zhou, H.; Liu, Q. PCN-222 MOF decorated conductive PEDOT films for sensitive electrochemical determination of chloramphenicol. *Mater. Chem. Phys.* **2021**, *270*, 124831. [[CrossRef](#)]
47. Laabd, M.; Imgharn, A.; Hsini, A.; Naciri, Y.; Mobarak, M.; Szunerits, S.; Boukherroub, R.; Albourine, A. Efficient detoxification of Cr(VI)-containing effluents by sequential adsorption and reduction using a novel cysteine-doped PANi@faujasite composite: Experimental study supported by advanced statistical physics prediction. *J. Hazard. Mater.* **2022**, *422*, 126857. [[CrossRef](#)]
48. Jiao, L.; Zhang, R.; Wan, G.; Yang, W.; Wan, X.; Zhou, H.; Shui, J.; Yu, S.-H.; Jiang, H.-L. Nanocasting SiO₂ into metal–organic frameworks imparts dual protection to high-loading Fe single-atom electrocatalysts. *Nat. Commun.* **2020**, *11*, 2831. [[CrossRef](#)]
49. Chai, L.; Wang, X.; Wu, D. Development of bifunctional microencapsulated phase change materials with crystalline titanium dioxide shell for latent-heat storage and photocatalytic effectiveness. *Appl. Energy* **2015**, *138*, 661–674. [[CrossRef](#)]

50. Liu, J.; Fan, Y.; Zhang, K.; Zhang, L.; Su, K.-Y. Engineering porphyrin metal–organic framework composites as multifunctional platforms for CO₂ adsorption and activation. *J. Am. Chem. Soc.* **2020**, *142*, 14548–14556. [[CrossRef](#)]
51. Liu, H.; Wang, X.; Wu, D. Fabrication of graphene/TiO₂/paraffin composite phase change materials for enhancement of solar energy efficiency in photocatalysis and latent heat storage. *ACS Sustain. Chem. Eng.* **2017**, *5*, 4906–4915. [[CrossRef](#)]
52. Zhao, Y.; Dong, Y.; Lu, F.; Ju, C.; Liu, L.; Zhang, J.; Zhang, B.; Feng, Y. Coordinative integration of a metal-porphyrinic framework and TiO₂ nanoparticles for the formation of composite photocatalysts with enhanced visible-light-driven photocatalytic activities. *J. Mater. Chem. A* **2017**, *5*, 15380–15389. [[CrossRef](#)]
53. Yuan, Y.P.; Yin, L.S.; Cao, S.W.; Xu, G.S.; Li, C.H.; Xue, C. Improving photocatalytic hydrogen production of metal-organic framework UiO-66 octahedrons by dye-sensitization. *Appl. Catal. B Environ.* **2015**, *168–169*, 572–576. [[CrossRef](#)]
54. Yao, K.; Liu, Y.; Yang, H.; Yuan, J.; Shan, S. Polyaniline-modified 3D-spongy SnS composites for the enhanced visible-light photocatalytic degradation of methyl orange. *Colloids Surfaces A* **2020**, *603*, 125240. [[CrossRef](#)]
55. Wang, L.; Jin, P.; Huang, J.; She, H.; Wang, Q. Integration of copper(ii)-porphyrin zirconium metal–organic framework and titanium dioxide to construct Z-scheme system for highly improved photocatalytic CO₂ reduction. *ACS Sustain. Chem. Eng.* **2019**, *7*, 15660–15670. [[CrossRef](#)]
56. Feng, D.; Gu, Z.-Y.; Li, J.-R.; Jiang, H.-L.; Wei, Z.; Zhou, H. Zirconium-metalloporphyrin PCN-222: Mesoporous metal-organic frameworks with ultrahigh stability as biomimetic catalysts. *Angew. Chem. Int. Ed.* **2012**, *51*, 10307–10310. [[CrossRef](#)]
57. Asano, N.; Uemura, S.; Kinugawa, T.; Akasaka, H.; Mizutani, T. Synthesis of biladienone and bilatrienone by coupled oxidation of tetraarylporphyrins. *J. Org. Chem.* **2007**, *72*, 5320–5326. [[CrossRef](#)]
58. Park, J.; Jiang, Q.; Feng, D.; Mao, L.; Zhou, H.-C. Size-controlled synthesis of porphyrinic metal–organic framework and functionalization for targeted photodynamic therapy. *J. Am. Chem. Soc.* **2016**, *138*, 3518–3525. [[CrossRef](#)]
59. Sami, S.; Etesami, N. Heat transfer enhancement of microencapsulated phase change material by addition of nanoparticles for a latent heat thermal energy storage system. *Energy Rep.* **2021**, *7*, 4930–4940. [[CrossRef](#)]
60. Zhai, D.; He, Y.; Zhang, X.; Li, W. Preparation, Morphology, and thermal performance of microencapsulated phase change materials with a MF/SiO₂ composite shell. *Energy Fuels* **2020**, *34*, 16819–16830. [[CrossRef](#)]
61. Parvate, S.; Singh, J.; Dixit, P.; Vennapusa, J.R.; Maiti, T.K.; Chattopadhyay, S. Titanium dioxide nanoparticle-decorated polymer microcapsules enclosing phase change material for thermal energy storage and photocatalysis. *ACS Appl. Polym. Mater.* **2021**, *3*, 1866–1879. [[CrossRef](#)]
62. Pornea, A.M.; Kim, H. Design and synthesis of SiO₂/TiO₂/PDA functionalized phase change microcapsules for efficient solar-driven energy storage. *Energ. Convers. Manag.* **2021**, *232*, 113801. [[CrossRef](#)]
63. Wang, H.; Luo, J.; Yang, Y.; Zhao, L.; Song, G.; Tang, G. Fabrication and characterization of microencapsulated phase change materials with an additional function of thermochromic performance. *Sol. Energy* **2016**, *139*, 591–598. [[CrossRef](#)]
64. Ruqaiya, A.N.; Guido, B.; Vladislavljjevic, G.T. Microfluidic production of poly(1,6-hexanediol diacrylate)-based polymer microspheres and bifunctional microcapsules with embedded TiO₂ nanoparticles. *Langmuir* **2018**, *34*, 11822–11831. [[CrossRef](#)]
65. Jiang, F.; Wang, X.; Wu, D. Design and synthesis of magnetic microcapsules based on *n*-eicosane core and Fe₃O₄/SiO₂ hybrid shell for dual-functional phase change materials. *Appl. Energy* **2014**, *134*, 456–468. [[CrossRef](#)]
66. Sun, N.; Xiao, Z. Paraffin wax-based phase change microencapsulation embedded with silicon nitride nanoparticles for thermal energy storage. *J. Mater. Sci.* **2016**, *51*, 8550–8561. [[CrossRef](#)]
67. Zhu, Y.; Chi, Y.; Liang, S.; Luo, X.; Chen, K.; Tian, C.; Wang, J.; Zhang, L. Novel metal coated nanoencapsulated phase change materials with high thermal conductivity for thermal energy storage. *Sol. Energy Mater. Sol. Cells* **2017**, *176*, 212–221. [[CrossRef](#)]
68. Zhao, Q.; He, F.; Zhang, Q.; Fan, J.; He, R.; Zhang, K.; Yan, H.; Yang, W. Microencapsulated phase change materials based on graphene Pickering emulsion for light-to-thermal energy conversion and management. *Sol. Energy Mater. Sol. Cells* **2019**, *203*, 110204. [[CrossRef](#)]
69. Wang, Z.; Ma, W.; Hu, D.; Wu, L. Synthesis and characterization of microencapsulated methyl laurate with polyurethane shell materials via interfacial polymerization in Pickering emulsions. *Colloids Surf. A Physicochem. Eng. Asp.* **2020**, *600*, 124958. [[CrossRef](#)]
70. Qiu, X.Z.; Tao, Y.; Xu, X.Q.; He, X.H.; Fu, X.Y. Synthesis and characterization of paraffin/TiO₂-P(MMA-co-BA) phase change material microcapsules for thermal energy storage. *J. Appl. Polym. Sci.* **2018**, *135*, 46447. [[CrossRef](#)]
71. Wang, H.; Zhao, L.; Song, G.; Tang, G.; Shi, X. Organic-inorganic hybrid shell microencapsulated phase change materials prepared from SiO₂/TiC-stabilized pickering emulsion polymerization. *Sol. Energy Mater. Sol. Cells* **2018**, *175*, 102–110. [[CrossRef](#)]
72. Ji, X.; Chen, J.; Dang, G.; Zhang, Y.; Yang, J.; Li, W.; Zhao, Y.; Jin, Z. Preparation of phase change microcapsules with inorganic/polymer hybrid shell through a “two-step” reaction. *Polym. Sci. Ser. B* **2019**, *61*, 560–566. [[CrossRef](#)]
73. Kuai, L.; Zhou, Y.; Tu, W.; Li, P.; Li, H.; Xu, Q.; Tang, L.; Wang, X.; Xiao, M.; Zou, Z. Rational construction of a CdS/reduced graphene oxide/TiO₂ core–shell nanostructure as an all-solid-state Z-scheme system for CO₂ photoreduction into solar fuels. *RSC Adv.* **2015**, *5*, 88409–88413. [[CrossRef](#)]
74. Takayama, T.; Sato, K.; Fujimura, T.; Kojima, Y.; Iwase, A.; Kudo, A. Photocatalytic CO₂ reduction using water as an electron donor by a powdered Z-scheme system consisting of metal sulfide and an RGO-TiO₂ composite. *Faraday Discuss.* **2017**, *198*, 397–407. [[CrossRef](#)] [[PubMed](#)]

75. Wang, C.; Liu, X.; He, W.; Zhao, Y.; Wei, Y.; Xiong, J.; Liu, J.; Li, J.; Song, W.; Zhang, X.; et al. All-solid-state Z-scheme photocatalysts of g-C₃N₄/Pt/macroporous-(TiO₂@carbon) for selective boosting visible-light-driven conversion of CO₂ to CH₄. *J. Catal.* **2020**, *389*, 440–449. [[CrossRef](#)]
76. Wang, C.; Zhao, Y.; Xu, H.; Li, Y.; Wei, Y.; Liu, J.; Zhao, Z. Efficient Z-scheme photocatalysts of ultrathin g-C₃N₄-wrapped Au/TiO₂-nanocrystals for enhanced visible-light-driven conversion of CO₂ with H₂O. *Appl. Catal. B Environ.* **2019**, *263*, 118314. [[CrossRef](#)]
77. Raza, A.; Shen, H.; Haidry, A.A.; Sun, L.; Liu, R.; Cui, S. Studies of Z-scheme WO₃-TiO₂/Cu₂ZnSnS₄ ternary nanocomposite with enhanced CO₂ photoreduction under visible light irradiation. *J. CO₂ Util.* **2020**, *37*, 260–271. [[CrossRef](#)]
78. Wei, Y.; Wu, X.; Zhao, Y.; Wang, L.; Zhao, Z.; Huang, X.; Liu, J.; Li, J. Efficient photocatalysts of TiO₂ nanocrystals-supported PtRu alloy nanoparticles for CO₂ reduction with H₂O: Synergistic effect of Pt-Ru. *Appl. Catal. B Environ.* **2018**, *236*, 445–457. [[CrossRef](#)]
79. Rodríguez, V.; Camarillo, R.; Martínez, F.; Jiménez, C.; Rincón, J. CO₂ photocatalytic reduction with CNT/TiO₂ based nanocomposites prepared by high-pressure technology. *J. Supercrit. Fluids* **2020**, *163*, 104876. [[CrossRef](#)]
80. Zhao, H.; Zheng, X.; Feng, X.; Li, Y. CO₂ Reduction by plasmonic Au nanoparticle-decorated TiO₂ photocatalyst with an ultrathin Al₂O₃ interlayer. *J. Phys. Chem. C* **2018**, *122*, 18949–18956. [[CrossRef](#)]